# Numerical Analysis of Fluid Flow in Rotating Micro-channels

A thesis submitted in partial fulfillment of the requirements for the award of the degree of
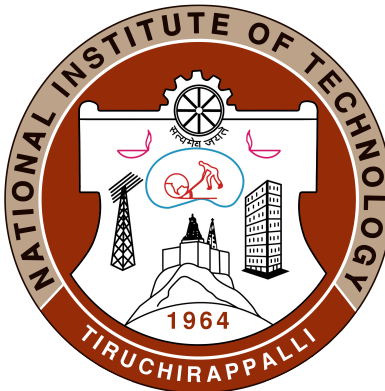
**Bachelor of Technology**

in

**Mechanical Engineering**

By

**Jagannath Suresh (111117041)**
**John S George (111117046)**
**Sameer A Dambal (111117076)**

# DEPARTMENT OF MECHANICAL ENGINEERING
# NATIONAL INSTITUTE OF TECHNOLOGY
# TIRUCHIRAPPALLI - 620015
## May 2021

# BONAFIDE CERTIFICATE

This is to certify that the project titled **"NUMERICAL ANALYSIS OF FLUID FLOW IN ROTATING MICRO-CHANNELS"** is a bonafide record of the work done by:

**Jagannath Suresh (111117041)**

**John S George (111117046)**

**Sameer A Dambal (111117076)**

in partial fulfillment of the requirements for the award of the degree

**BACHELOR OF TECHNOLOGY** in **MECHANICAL ENGINEERING**

at the **NATIONAL INSTITUTE OF TECHNOLOGY, TIRUCHIRAPPALLI,**

during the year 2020-2021.

**Dr. Kaushik P**
(Project Guide)

**Dr. AR. Veerappan**
(Head of the Department)

Project viva-voce held on: _____

**Internal Examiner**

**External Examiner**

# 1 ABSTRACT

Fluid flow investigation in rotating micro-channels is a pivotal area of study in centrifugal microfluidics, which has also recently emerged as an important technique in chemical separations and biomedical applications. The rotation brings in the coriolis force and centrifugal force which goes on to affect the flow pattern in a rotating micro-channel significantly compared to a non rotating channel. Effective control of mixing and flow pattern within a centrifugal microfluidic device is an important aspect of its design and in this work, we do a comprehensive numerical study of the flow pattern in a rotating micro-channel along the development of the flow.

A pressure based finite volume technique with a collocated grid was used to solve the Navier Stokes equations in a non-inertial frame using C++. SIMPLE algorithm was implemented for pressure velocity coupling and the Rhie-Chow interpolation scheme was used to implement the algorithm on the non-staggered grid. The discretised linear equations were solved using the CGSTAB solver till convergence was achieved. The code implemented was further validated by implementing the flow for a non-rotating pipe and comparing the results with the analytical results. The validated code was then used to do the numerical study for a micro-channel with rotation and the resulting data points of the grid were plotted using MATLAB and GNUplot. The results for the rotating micro-channel was found to have irregularities as the rotational Reynolds number was increased due to the high secondary flow and the same has been depicted in this thesis.

As an extension of this project work, the outlet boundary conditions are being changed to negate the irregularities and to check if the fluid flow fully develops throughout its course. We will be trying to arrive at a relation to find the entry length in a rotating channel with the help of Buckingham pi theorem and regression analysis in the future. Any mixing prevelant in the micro-channel will also be investigated further.

# 2 ACKNOWLEDGMENTS

It is a genuine pleasure to express our deep sense of gratitude to our mentor, **Dr. Kaushik P, Assistant Professor, Mechanical Engineering** at the National Institute of Technology Tiruchirappalli. His utmost dedication, support and motivation at every step of the way has proved to be pivotal in conducting this study. His prompt responses to advice us numerous times over several months helped us expedite the completion of this project.

We also thank the Mechanical Engineering Department and all its faculty members for their efforts to equip us with the skills needed to work on this research problem.

We would like to thank the National Institute of Technology Tiruchirappalli for providing us with ample opportunities and a conducive environment to work on our skills that culminated in the completion of this thesis.

Finally, we would like to thank our parents, guardians and friends for constantly supporting us and for providing us with opportunities to grow in our careers.

# Contents

# List of Tables

# List of Figures

# Nomenclature

$\alpha_P$ — Pressure under relaxation

$\alpha_u$ — X velocity under relaxation

$\forall$ — Volume of the control volume

$\Gamma$ — Diffusion Coefficient

$\mu$ — Dynamic Viscosity

$\rho$ — Density

$B_u$ — Body Force

$D_h$ — Hydrodynamic Diameter

$d_r$ — Distance from disk centre to micro-channel inlet

$f_\omega$ — Centrifugal Force

$f_c$ — Coriolis Force

$L_h$ — Hydrodynamic entrance length

$P^*$ — Guessed Pressure

$r'$ — Position vector relative to rotating frame

$R_0$ — Initial value of Euclidean norm of residual

$R_f$ — Reduction Factor

$R_{ext.loop}$ — Euclidean norm of pressure correction residual

$R_{internalloop}$ — Euclidean norm of momentum residual

$Re_\omega$ — Rotational Reynolds Number

$V'$ — Velocity relative to rotating frame

$w_{avg}$ — Average axial velocity

$w_{in}$ — Inlet velocity

$\dot{m}_{imbalance}$ — Mass flow imbalance

$\omega$ — Angular Velocity

A — Area of control volume face

| | |
|---|---|
| D | Diffusion Strength |
| F | Advection Strength |
| Kn | Knudsen Number |
| m | Mass |
| P | Pressure |
| Pe | Peclet Number |
| Re | Reynolds Number |
| Res | Residual |
| S | Source term |
| T | Temperature |
| Tol | Tolerance |
| u | Velocity in the X direction |
| v | Velocity in the Y direction |
| w | Velocity in the Z direction |

# 3   INTRODUCTION

## 3.1   Overview

The study of fluid flow in micro-channels has been pivotal as it finds useful application in several industries. Analysis [1], experimentation and research of fluid flow and mixing in rotating micro-channels is critical for centrifugally actuated microfluidic devices. They have ubiquitous applications in chemical analysis, biomedical applications and most importantly, in drug delivery. The current study models the fluid flow in similar micro-channels. However, we aim to probe the implications of rotating the micro-channel and understand how the rotation speed, Reynolds number, rotational Reynolds number and other parameters affect the potential mixing ability of the microdevice. To illustrate this, we will first attempt to illustrate how a general microchip is constructed and how it functions.

An array of microchannels is etched on a compact circular disk substrate which is then rotated at a constant frequency. By controlling this frequency, mixing, separation, routing, valving, siphoning, and droplet generation can be performed efficiently. This is called as a Lab-on-a-CD (LabCD). The objective of this compact disk like platform is to combine multiple liquid handling steps in order to perform all the bio-chemical processes in a flexible way. A successful design of centrifugal microfluidic devices requires a coherent understanding of fluid flow inside these rotating microchannels.

The physics of fluid flow through rotating microchannels is primarily governed by the *pseudo forces*, namely the **centrifugal and the Coriolis forces**, arising as a manifestation of expressing the governing equations in a rotating reference frame. At small rotation speeds, the flow is purely driven by the *centrifugal force*. At higher rotation, the *Coriolis force* dominates and a significant secondary flow can be observed perpendicular to the primary flow velocity. The effective operation of a centrifugal microfluidic platform depends on regulating these forces in a controlled manner. For example, the working principle of capillary burst valve depends on the balance of centrifugal force and surface tension force. On the other hand, mixing is enhanced in microchannels when the Coriolis force dominates over the centrifugal force. The process becomes more complicated when heat transfer is included in the scenario. In some cases it is necessary to maintain the fluid within specific temperature ranges while rotating it inside the microchannel. For instance, the polymerase chain reaction (PCR) needs thermal homogeneity for efficient DNA hybridization. In order to compute the correct temperature distribution of the fluid inside a rotating microchannel, the effect of rotation on convective heat transfer should be taken into consideration.

The flow physics in microscale can be modeled in two ways –

- Assuming it as a continuous medium with spatial and temporal variations of macroscopic flow quantities such as velocity, pressure, temperature or density.

- By treating it as a collection of discrete particles whose flow properties are obtained

by deterministic or probabilistic approaches

The continuum hypothesis validates the Navier-Stokes equations to adequately describe the physics of flow inside microchannels. The *Knudsen number (Kn)* is used as a validity indicator of the continuum hypothesis assumption. It is given by the ratio of the mean free path of the fluid molecules to the characteristic length. For $Kn < 0.01$, the fluid is a continuum. As the Knudsen number approaches unity, the continuum equations tend to fail. However, for $Kn < 0.1$, the no slip boundary condition can be cleverly adjusted using a slip parameter. The region $0.01 < Kn < 0.1$, also known as the *slip regime* differs from the transition regime $0.1 < Kn < 10$. In the slip region, the Boltzmann equations are solved directly to predict flows.

For biological liquids, such as blood, plasma, and for water, $Kn$ falls within the continuum region. The NS equations with no slip boundary conditions are applicable for any range of the microchannel. Analyses based on NS and energy equations can predict the flow in microchannels having a hydraulic diameter greater than 50 m, provided that the experimental conditions and measurements are correctly identified and simulated. If the continuum hypothesis is also valid for centrifugally driven micro-flows, then the analysis of flow and heat transfer will not differ from that in rotating macro sized channels.

Micro-scale technology plays a significant role for design and development of efficient reactors, mixers and separation devices. In this regard, microfluidic channels are efficiently used for controlled mixing, separation and reaction purposes. The available high surface to volume ratio of such microfluidic system helps to improve the rate of heat and mass transfer associated to any chemical process and it facilitates the compact designing of the process.

## 3.2   Potential Applications:

Present day microfluidics can be traced back to the fabrication of a chromatograph which was a silicon chip and the ink-jet printer. Since that time, the field has burgeoned and diversified into many disparate fields. Some of the significant applications are in **Biological and Chemical Analysis**, **Clinical and Forensic Analysis Medical Diagnostics**, **Molecular Diagnostics**, etc.

**Growing market for rotating microfluidic platforms in biomedical applications:**

A microfluidic device includes in it many pertinent parts and utility of a typical room-sized laboratory on to a small chip. Examples include devices with on-chip temperature control and gradient generation for use with heterogeneous DNA hybridization. The most significant benefit of these lab-on-a-chip devices would be the analytical improvements associated with the scaling down of the size. Further literature survey reveals other critical advantages like minimized consumption of reagents, increased automation and reduced manufacturing costs. As this drifts from the relatively complex silicon and glass based micro machining originally

developed in the electronics industry, this is perhaps the most important development. As these manufacturing technologies are further and further advanced (both in terms of the potential complexity of an integrated device and the ease with which a simple prototype can be made) in parallel with analytical needs, the development of future integrated devices will inevitably be less expensive and faster than ever before.

## 3.3    Literature Review:

Before beginning with our study, we conducted a thorough literature review to understand the status quo in the field of microfluidics. Our goal was to use established knowledge in this field and extend it to our study to measure the entry length of our rotating microchannel. Once this was done, our goal was to use our program to comfortably analyse fluid mixing properties in the fully developed region in our microchannels. In lieu of this motivation, we perused primarily through the literature as cited in the reference.

**Review of the field of microfluidics:**

This field deals [2] with fluid-handling technologies where atleast one of the dimensions of the device at hand is less that $1mm$. As explained above, it finds a plethora of applications in ink-jet printers, synthetic chemistry among others.

In microchannels width $> 10\mu m$, the motion of solute is often slow by diffusion across the laminar flow. Thus mixing is generally regarded as a slow process. However, this can be overcome by incorporating transverse flows that stir the fluid. A chaotic flow is defined as a stirring technique wherein the flow stretches and folds the fluid in such a way that the interface between unmixed regions grows exponentially with time [3].

Active mixers create transverse motion in the principal flow, with local, oscillatory forces generated with bubbles, applied electric or magnetic fields, or flows in cross-channels. Active mixers have the potential to be very efficient, but require sophisticated controls. Passive mixers use fixed geometrical features in the channel to induce transverse components in the principal flow; for an example, [4]. These designs are simple to operate but may not achieve full mixing as quickly as active designs.

# 4    MATHEMATICAL MODELLING

## 4.1    Working Principle

In most of the centrifugal microfluidic devices, a microchamber in the centre of the disk houses the fluid which is connected to the essential reservoirs through micro-channels. Figure 1 shows a schematic diagram of an array of rectangular micro-channels arranged radially on a sector of a rotating circular disk (the actual arrangement would consist of similar channels throughout the disk). As the disk is considered to be rotating around an axis perpendicular to the plane of the disk, a centrifugal force $f_\omega$ acts radially outward hence pushing the incoming fluid from the microchamber to the reservoir through the micro-channel. At the initial stage when the first trace of the fluid enters the channel, the velocity and the shape of the liquid meniscus is governed primarily by the centrifugal force and the surface tension force. But, in this study we are considering a micro-channel in which the liquid flow has been established already and henceforth, the surface tension force can be neglected. Apart from the centrifugal force, another force that arises due to the rotation is the coriolis force $f_c$ which acts in a direction perpendicular to the centrifugal force along the plane of the disk. This coriolis force which is induced due to the rotation is responsible for the recirculation accompanying the secondary flow phenomena which can be observed in a rotating micro-channel flow.
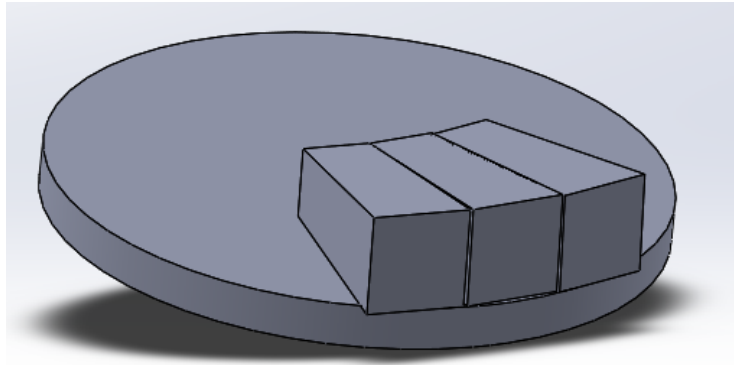


Figure 1: A sector of the disk arranged with micro-channels(Figure not to scale)

In physics, the coriolis force $f_c$ is an inertial force that acts on objects that are in motion within a rotating frame of reference. In the current study, we consider the disk to be rotating in an anti-clockwise direction (fig 2) and henceforth, the force acts to the left of the motion of the object. And the centrifugal force $f_\omega$ is another inertial force which acts on objects in a rotating frame of reference. This force acts away from the axis of rotation and also passes through the coordinate system's origin.

These inertial forces acts as additional forces in the rotating frame that contributes to the apparent acceleration like the real forces. The equations to calculate these forces are expressed below:

- **Coriolis Force** - $2\mathrm{m}\left(\omega \times \mathrm{v'}\right)$

- **Centrifugal Force** - $\mathrm{m}\omega \times\left(\omega \times \mathrm{r'}\right)$

where,
$\omega$ is the angular velocity, of the rotating reference frame relative to the inertial frame.
$v'$ is the velocity relative to the rotating reference frame.
$r'$ is the position vector of the object relative to the rotating reference frame.

Two non-dimensional numbers, namely the Reynolds number (Re) and the Rotational Reynolds number $(Re_\omega)$ helps in explaining the physics of rotating channel flows.

- **Reynolds number** $= \dfrac{\rho w_{avg} D_h}{\mu} = \dfrac{Inertial Force}{Viscous Force}$

- **Rotational Reynolds number** $= \dfrac{\rho \omega {D_h}^2}{\mu} = \dfrac{Rotational Force}{Viscous Force}$

A parabolic axial velocity profile is assumed in the flow direction and Pratanu Roy et al. [1] calculated the ratio of Coriolis Force($f_c$) and the centrifugal force($f_\omega$) and it was found out to be a multiple of the Rotational Reynolds number($Re_\omega$). Hence, it can be inferred that a high Rotational Reynolds number will induce a high Coriolis force in turn resulting in a strong secondary flow.

## 4.2   Geometry and Independent Parameters

In the present work, we are looking at the dynamics of flow in an array of radially aligned rectangular micro-channels on a circular disk. The inlet of the micro-channel is located at a distance $d_r$ from the centre of the disk which is assigned a value of 20mm as depicted in Figure 2. Since the array of micro-channels follows a repetitive framework, the flow is expected to develop in the same fashion in all the micro-channels. Henceforth, the problem can be simplified by using just one micro-channel as the solution domain. Since the angle between successive micro-channels is significantly small, each single micro-channel can be approximated as a straight rectangular channel which as mentioned above is also our solution domain. The disk rotates at $\omega$ RPM and corresponding to the same, two forces act on the fluid domain, namely the coriolis force $f_c$ and the centrifugal force $f_\omega$ in mutually
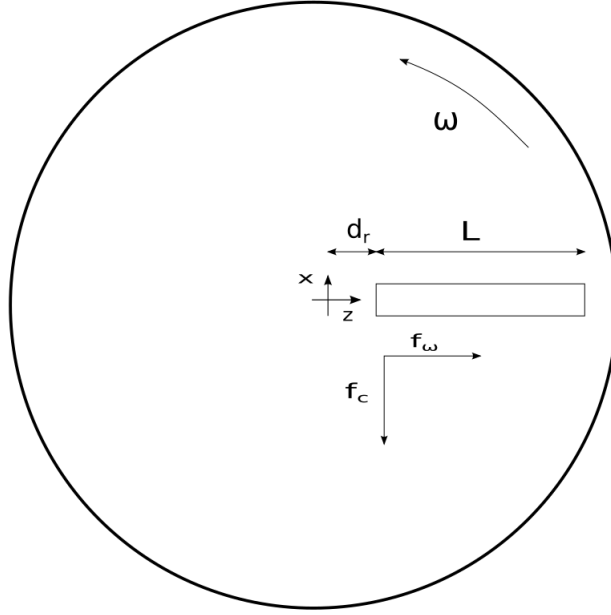
Figure 2: A schematic diagram of the rotating disk with a single micro-channel - Top View

perpendicular directions.The orientation of the solution domain and the corresponding co-ordinate system is depicted in Figure 3.

As shown in the figure, the X-Y plane houses a square face with a side length a=0.2mm in the case of the micro-channel. And, the length of the micro-channel along the Z direction is b=20mm. The rotation of the channel takes place about the Y axis in the clockwise direction.

## 4.3   Governing Equations

The flow in the micro-channel is taken to be in the laminar region given that the hydraulic diameter of the micro-channel is $D_h = 0.2mm$ and the range of inlet velocities are also taken in such a way that the Reynolds Number($R_e$) falls well within the laminar regime. Since the primary objective of the numerical study is to understand the development of the velocity and pressure fields in the rotating micro-channel, the governing equations for the study are the equations of continuity and momentum conservation for a three dimensional unsteady, laminar and incompressible flow which are expressed below:

- **Continuity Equation**

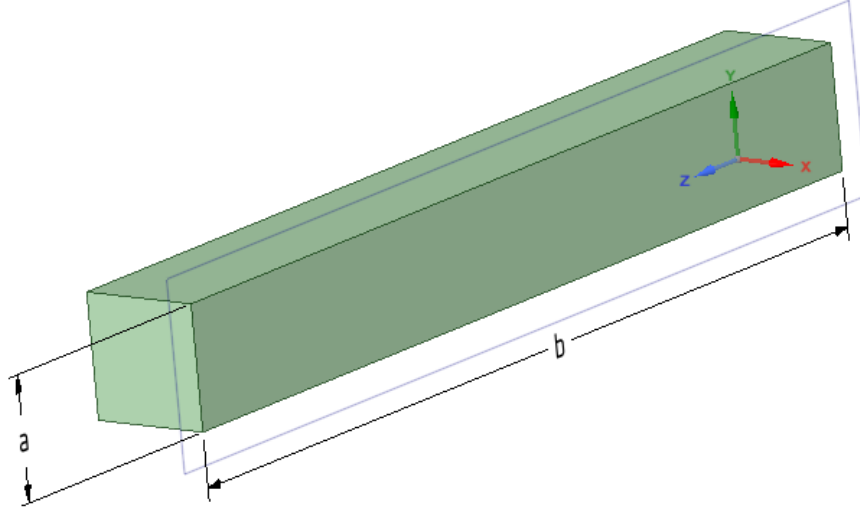$$\rho[\frac{\partial u}{\partial x} + \frac{\partial v}{\partial y} + \frac{\partial w}{\partial z}] \tag{1}$$

Figure 3: Geometry of the model problem

- **X Momentum Equation**

$$\rho\frac{\partial u}{\partial t} + \rho[u\frac{\partial u}{\partial x} + v\frac{\partial u}{\partial y} + w\frac{\partial u}{\partial z}] = \mu[\frac{\partial^2 u}{\partial x^2} + \frac{\partial^2 u}{\partial y^2} + \frac{\partial^2 u}{\partial z^2}] + (\rho\omega^2 x - 2\rho\omega w) - \frac{\partial p}{\partial x}$$
(2)

- **Y Momentum Equation**

$$\rho\frac{\partial v}{\partial t} + \rho[u\frac{\partial v}{\partial x} + v\frac{\partial v}{\partial y} + w\frac{\partial v}{\partial z}] = \mu[\frac{\partial^2 v}{\partial x^2} + \frac{\partial^2 v}{\partial y^2} + \frac{\partial^2 v}{\partial z^2}] - \frac{\partial p}{\partial y}$$
(3)

- **Z Momentum Equation**

$$\rho\frac{\partial w}{\partial t} + \rho[u\frac{\partial w}{\partial x} + v\frac{\partial w}{\partial y} + w\frac{\partial w}{\partial z}] = \mu[\frac{\partial^2 w}{\partial x^2} + \frac{\partial^2 w}{\partial y^2} + \frac{\partial^2 w}{\partial z^2}] + (\rho\omega^2 z + 2\rho\omega u) - \frac{\partial p}{\partial z}$$
(4)

Due to the rotation of the micro-channel, additional forces namely the centrifugal force and the coriolis force affects the dynamics of the flow as explained earlier. We solve the equations from a non inertial frame of reference and hence the coriolis force and the centrifugal force comes in as the source terms. We also assume the gravity effects to be negligible and the flow to be isothermal. The present study was intended to be solved in an unsteady condition as expressed in the governing equations above, but due to constraints with computational

power and resources, the study has been limited to a steady state analysis.

## 4.4   Boundary Conditions

A set of equations used along a domain boundary to obtain a particular solution to the problem is called a boundary condition. The equation solved and it's known variables influence the boundary condition for a given physical condition. For example on a physical "Wall", the boundary condition for the momentum equation could be a slip or a no-slip condition, while for the energy equation it could be a specified flux, an imposed temperature, or a convection heat transfer condition. The general categories of boundary conditions are mentioned below:

- a Dirichlet condition, where the unknown variable is defined at the boundary;

- a von Neumann condition, where the flux expressed in the conservation equation is defined at the boundary face;

- a Robin-type condition, where the unknown variable and flux at the boundary are expressed via a constitutive relation

The boundary conditions we use in the present study are [5]:

1. **No-Slip Boundary Condition** - This condition assumes that the speed of the liquid in contact with the boundary is equal to the velocity of the boundary which is zero in this study as we consider a stationary wall. The relative movement between the boundary and the fluid layer in contact with the boundary is zero and hence the name "no-slip condition".
   Since the mass flow rate is zero at the walls, the mass imbalance is also zero in the pressure correction equation and no modifications are required. The pressure at the boundary is obtained by linear extrapolation from the neighbouring 2 nodes of the field near the boundary.

2. **Specified Velocity** - The velocity is specified at the inlet and it also implies a known mass flux. The inlet in this case is through the back face as shown in figure 6. The pressure at the boundary is linearly extrapolated similar to no-slip boundary conditions.

3. **Specified Pressure** - The pressure at the outlet boundary is specified in this case. We use the gauge pressure in this case and it was set to zero in the outlet.
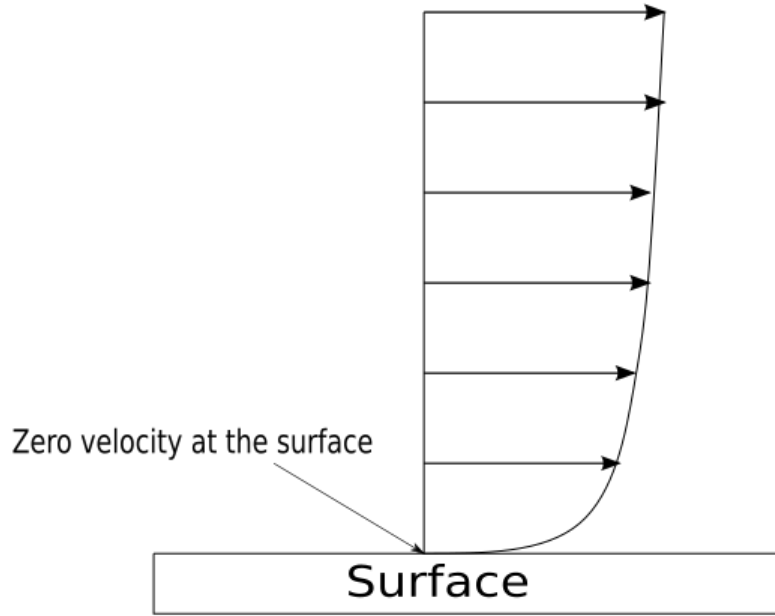
Figure 4: No slip condition besides a wall

The benefits of using gauge pressure over absolute pressure in CFD calculations are the following:

- The vast majority of CFD calculations are performed at pressures close to 1 atm ($1.01325 \times 10^5$ Pa), rather than near vacuum (0 atm).

- In contrast, the pressure drop in most engineering applications is a few tens of Pa at most, especially for gas flow.

- Small changes in pressure tend to get lost in numerical precision errors if we deal with numbers as large as  $10^5$.

**Note** - Later on in the study, the specified pressure boundary condition was found to cause irregularities in the outlet flow because of the secondary flow induced due to the rotation of the micro-channel. Hence, the outlet boundary condition is being changed from a constant pressure condition to an outflow condition and will not be included in this report due to limitations with computational power as the work is happening remotely due to COVID-19. Hence, the alteration that is being made will be part of the future work.

# 5 NUMERICAL SOLUTION

A finite volume technique was used to discretise the governing equations. We deal with 4 governing equations namely, the continuity equation and the momentum equations in the X, Y and Z directions. As explained earlier, we are interested in finding the velocity (u,v and w) and pressure (p) along the channel flow. Hence, we have 4 unknowns and 4 equations to solve. From the governing equations, it can be seen that all 4 unknowns appear in the momentum equations, but the continuity equation only has 3 of the 4 unknowns. Since the X momentum equation represents force balance in the X direction (Newton's second law), it follows that it is the governing equation that would be solved to determine u. Similarly, the Y momentum equation and the Z momentum equation would be solved to determine v and w respectively. And hence ideally, the solving the continuity equation should give the pressure but p is not present in the equation. Hence pressure velocity coupling has to be obtained from the combination of the continuity equation and the equations of momentum through a special algorithm named SIMPLE and the same was followed in the present study. The codes for the solution were written in C++.

## 5.1 Choice of Grid

One of the quantities that is key to Finite Volume formulations for the fluid flow equations is the mass flux across cell faces. And, to compute the mass flux at cell faces, we need velocities at cell faces. Unfortunately, in a normal grid the velocities are calculated at cell centres, not faces and calculation of cell face velocities from cell centre velocities requires some kind of interpolation. Unfortunately, early researchers in CFD found that if standard distance weighted interpolation is used, the resulting solution flip-flops between two or more solutions which is also called checkerboard pressure oscillations [6]. The nature of this oscillation is shown in [7] for structured Cartesian grids and in [8] for unstructured grids. The staggered grid was proposed to counter the issue of checkerboard pressure oscillations which uses different control volumes for momentum and continuity equations and eliminates interpolation of cell centre velocities to find the face velocities.

Even though the staggered grid helps negate the checkerboard pressure oscillations, in the present study we use the collocated grid with a special interpolation scheme named the Rhie-Chow interpolation [9] to discretise the equations as the staggered grid was found to have multiple disadvantages with respect to this study and the same are mentioned below:

- Book-keeping is difficult and tedious

- Boundary conditions are difficult to implement (has to be done separately for each independent variable

- Interpolation is counter intuitive

The main difference between staggered and collocated is that with the collocated grid all variables are located on the same points of the grid. On the other hand, the components of the velocity vectors are represented at staggered points in the respective directions between two adjacent pressure points. And, on a 3D staggered grid, it is essential to define four control volumes to calculate u,v,w, and p wheres a collocated grid can be used to solve the same equations with just one control volume.Also the momentum conservation is guaranteed for the entire control volume in a collocated grid which is not often the case with the staggered grid as the conservation law is generally only guaranteed over 25% of the control volume.

A detailed comparison between staggered and collocated grids in the finite volume method is shown in [10].

## 5.2   Discretisation

The key step of the finite volume method is the integration of the governing equation over a control volume to yield a discretised equation at it's nodal point P. The control volume and it's conventions used in the present study is depicted in Figure 5.

To arrive at a general discretised equation, we currently the 3D convection-diffusion equation portraying the steady transport of a property $\phi$ which is given by:

$$\nabla \cdot (\rho u \phi) = \nabla \cdot (\Gamma \nabla \phi) + S_\phi \tag{5}$$

Steady three dimensional convection diffusion of a general property $\phi$ in a velocity field $\mathbf{u}$ is governed by

$$\frac{\partial(\rho u \phi)}{\partial x} + \frac{\partial(\rho v \phi)}{\partial y} + \frac{\partial(\rho w \phi)}{\partial z} = \frac{\partial}{\partial x}(\Gamma \frac{\partial \phi}{\partial x}) + \frac{\partial}{\partial y}(\Gamma \frac{\partial \phi}{\partial y}) + \frac{\partial}{\partial z}(\Gamma \frac{\partial \phi}{\partial z}) + S \tag{6}$$

**Hybrid differencing scheme** was chosen over the central and upwind differencing schemes to discretise the 3D convection-diffusion equation mentioned above. The central and upwind differencing schemes were identified to have multiple disadvantages while solving convection-diffusion equations which are mentioned below respectively:

**Note - Peclet Number (Pe)** is a dimensionless number given by:

- $\text{Pe} = \frac{advective\ transport\ rate}{diffusive\ transport\ rate} = \frac{F}{D}$
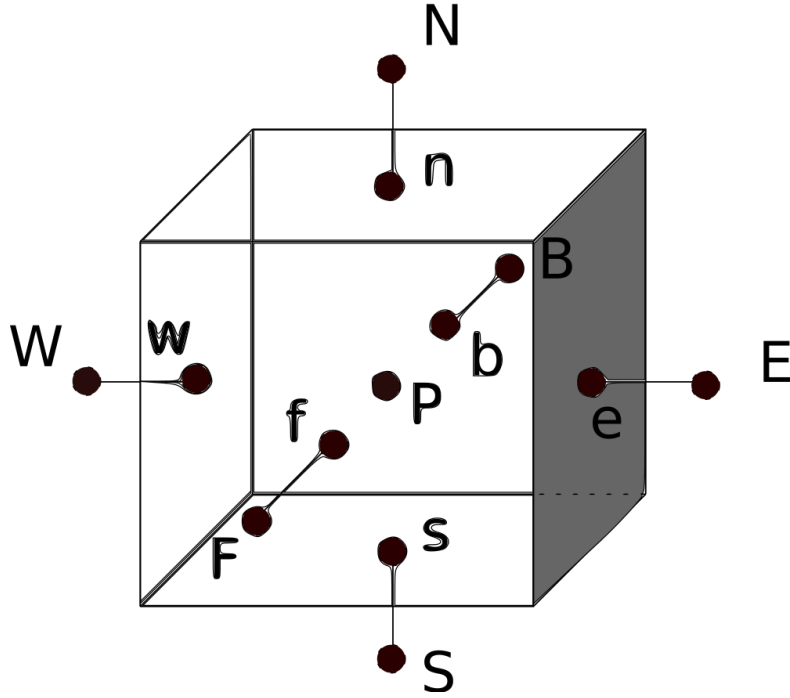
Figure 5: A single control volume

It helps in identifying whether the flow is advection or diffusion dominant. Generally, if the Peclet number is less than 2, the flow is considered to be diffusion dominant and if it is more than 2, it is considered to be advection dominant. The Peclet number of a single cell is called the cell Peclet number.

- **Central Differencing Scheme**

  The central differencing scheme introduces influencing at the central node from the directions of all its neighbours to calculate the convective and diffusive flux. Thus the scheme does not recognise the direction of the flow or the strength of convection relative to diffusion. It does not possess the transportiveness property at high Pe. This scheme will only be stable and accurate if the Peclet number Pe of the flow is less than 2 (Pe < 2). The Scarborough criterion might also not be satisfied when central differencing scheme is used for high Peclet number flows. Owing to this limitation central differencing scheme is not a suitable discretisation practice for general-purpose flow calculations.

- **Upwind Differencing Scheme**

  One of the major inadequacies of the central differencing scheme is its inability to identify flow direction. This drawback is negated in the upwind scheme as the convected value of $\phi$ at a cell face is taken to be equal to the value at the upstream node. Since

it is a flow dominant differencing scheme, it works well predominantly for high Peclet number flows i.e. generally when the Peclet number is less than 2 (Pe > 2). Hence, it is not very suitable for diffusion dominated or low Peclet number flows.

Since the flow in the present study has a reasonably wide range of cell Peclet numbers over the grid, the hybrid differencing scheme of Spalding (1972) is used which is based on a combination of central and upwind differencing schemes. The central differencing scheme, which is second-order accurate, is employed for small Peclet numbers (Pe < 2) and the upwind scheme, which is first-order accurate but accounts for transportiveness, is employed for large Peclet numbers (Pe ≥ 2).

For instance, the hybrid differencing formula for the net flux per unit area through the west face of the control volume is as follows:

$$q_w = F_w[\frac{1}{2}(1 + \frac{2}{Pe_w})\phi_W + \frac{1}{2}(1 - \frac{2}{Pe_w})\phi_P] \qquad for -2 < Pe_w < 2 \qquad (7)$$

$$q_w = F_w\phi_W \qquad for \quad Pe_w \geq 2 \qquad (8)$$

$$q_w = F_w\phi_P \qquad for \quad Pe_w \leq -2 \qquad (9)$$

The fully implicit discretisation equation is:

$$a_P\phi_P = a_W\phi_W + a_E\phi_E + a_S\phi_S + a_N\phi_N + a_B\phi_B + a_F\phi_F + S \qquad (10)$$

The discretised source term $S_u$ for the X, Y and Z momentum equations are different based on equations 2-4 and the same is mentioned below:

- **X momentum equation**

$$(S)_x = \frac{\rho\omega^2}{2}[x_e{}^2 - x_w{}^2]A_e - 2\rho\omega w_p\forall + \frac{A_e}{2}(P_W{}^* - P_E{}^*) \qquad (11)$$

- **Y momentum equation**

$$(S)_y = \frac{A_n}{2}(P_S{}^* - P_N{}^*) \qquad (12)$$

- **Z momentum equation**

$$(S)_z = \frac{\rho\omega^2}{2}[z_f{}^2 - z_b{}^2]A_t + 2\rho\omega u_p \forall + \frac{A_f}{2}(P_B{}^* - P_F{}^*) \qquad (13)$$

where,

1. $A_e = A_w =$ Area of east/west face

2. $A_n = A_s =$ Area of north/south face

3. $A_f = A_b =$ Area of front/back face

4. $\forall =$ Volume of the control volume

5. $P_W{}^*$, $P_E{}^*$, $P_S{}^*$, $P_N{}^*$, $P_B{}^*$, and $P_F{}^*$ are the guessed pressures on the west, east, south, north, back, and front faces respectively

The values of the link coefficients $a_P$, $a_W$, $a_E$, $a_S$, $a_N$, $a_B$ and $a_F$ can be found out with standard hybrid differencing formulas as mentioned in [11].

## 5.3   Algorithm and Accompanying Procedures
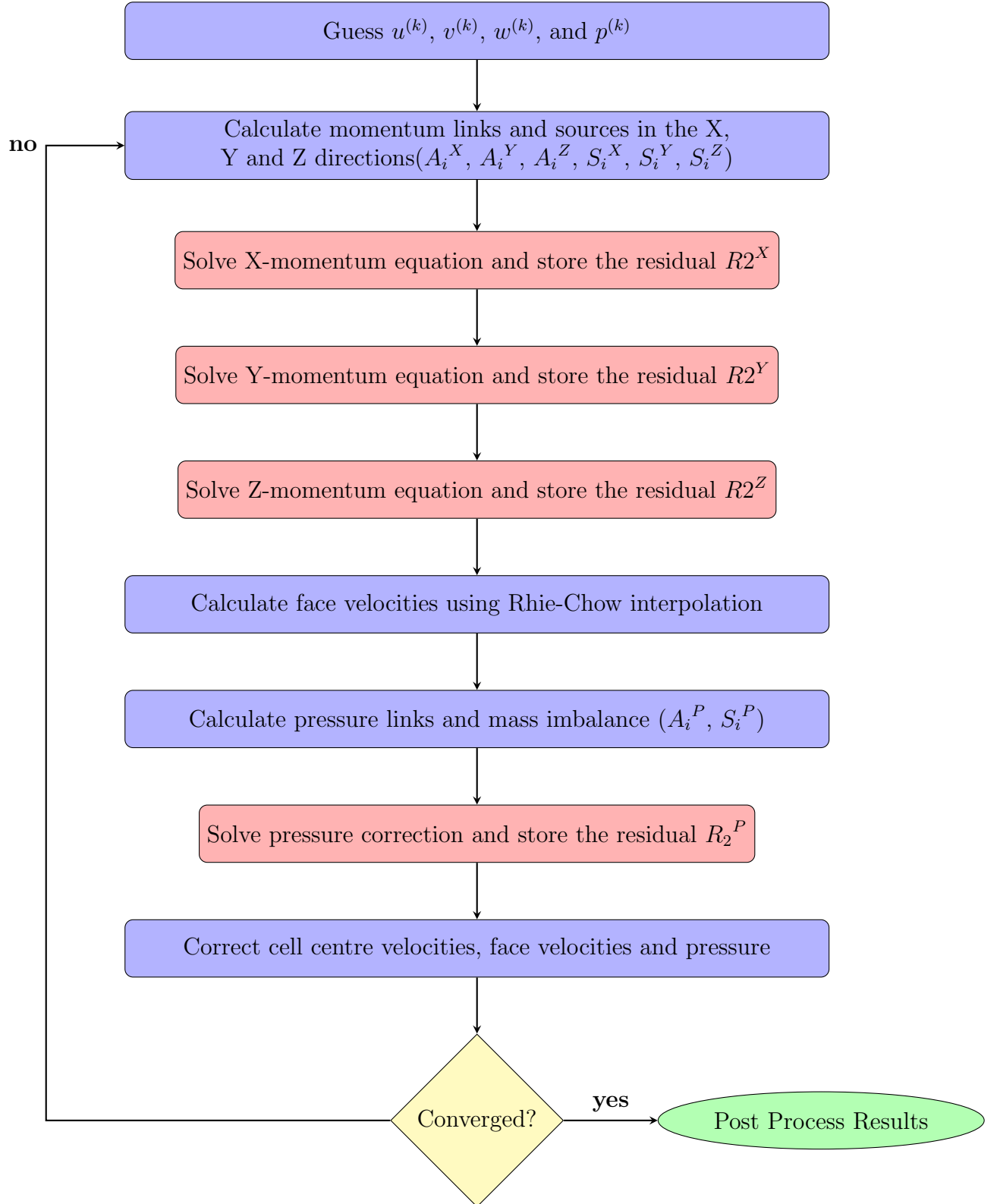


In the present study, SIMPLE algorithm (Semi-Implicit Method for Pressure Linked Equa-

tions) was used to solve the discretised governing equations. The algorithm was originally put forward by Patankar et al. and Spalding et al. [12] in 1972 and is essentially a guess and correct procedure. The stepwise procedure followed in SIMPLE algorithm on the collocated mesh is shown above.

The pressure correction equation mentioned above, is derived from the continuity equation and is used to solve for the pressure. The equation is derived by integrating the continuity equation over the control volume and substituting the corrected face velocity expressions which contains the pressure correction terms as shown in [13].

The pressure correction equation is given by:

$$A_p P_p{}' + A_W P_W{}' + A_E P_E{}' + A_S P_S{}' + A_N P_N{}' + A_F P_F{}' + A_B P_B{}' = S^p = -\dot{m}_{imbalance}$$

(14)

and,

$$\dot{m}_{imbalance} = \rho(u_e - u_w)\Delta y \Delta z + \rho(v_n - v_s)\Delta x \Delta z + \rho(w_f - w_b)\Delta x \Delta y \quad (15)$$

where,
$u_e$, $u_w$, $v_n$, $v_s$, $w_f$ and $w_b$ are the face velocities of the respective faces of the control volume as shown in figure 5.

The calculation of the mass imbalance requires the values of the face velocities of the control volume. Unlike a staggered grid, where the face velocities would be readily available, in a collocated grid an interpolation scheme to calculate the face velocities is necessary and hence, we use the Rhie-Chow interpolation scheme which is explained in the next section.

### 5.3.1   Rhie Chow Interpolation

The most significant weakness of collocated grid discretisations is that they inherently admit checkerboard pressure oscillations. Hence to negate this problem, this interpolation method was developed by Rhie and Chow [14] and since then it has been widely used because of it's simple algorithm especially for non staggered grids. Normal distance weighted interpolation to find the face velocities will not give good results and does not negate the problem of checkerboard pressure oscillations. In the Rhie and Chow scheme, the momentum equations are solved at the cell-centered locations and the resulting velocity is further interpolated to find the face velocities. The discrete mass conservation equation is expressed in terms of the discrete mass fluxes across cell faces and this technique is forced to imitate a staggered grid discretisation. This technique also eliminates the pressure velocity decoupling.

For simplicity of expression, currently considering the velocity in the X direction as shown in figure 6. The discretised momentum equation for the cell-centered velocity component

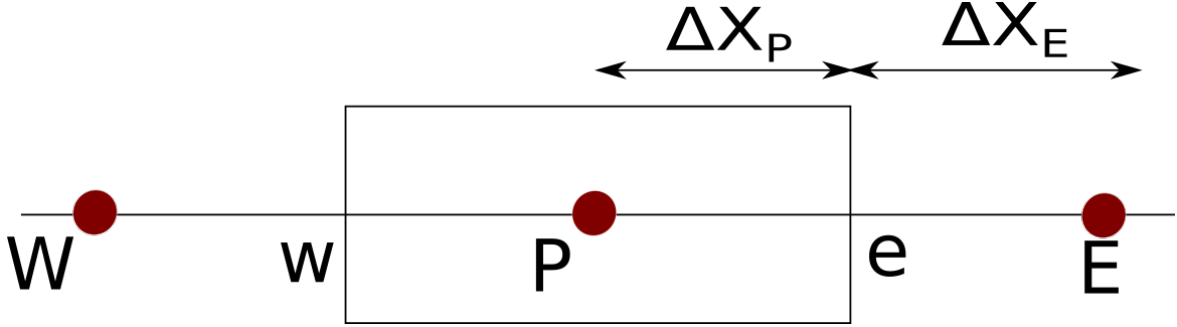can be written as follows, with the under-relaxation factors and body force terms expressed explicitly:



Figure 6: Computational stencil and node locations in the X direction

$$u_P = (H_u)_P + (D_u)_P(P_w - P_e) + (B_u)_P + (1 - \alpha_u){u_P}^{k-1} \qquad (16)$$

where

$$H_u = \frac{\alpha_u[\Sigma A_{nb}{}^u u_{nb}]}{A_P{}^u} \qquad (17)$$

$$D_u = \frac{\alpha_u \Delta y \Delta z}{A_P{}^u} \qquad (18)$$

$$B_u = \frac{\alpha_u S_u{}^{body} \Delta V}{A_P{}^u} \qquad (19)$$

Hence, the discretized form of momentum equation for the cell-face velocity components can be written as follows:

$$u_e = (H_u)_e + (D_u)_e(P_P - P_E) + (B_u)_e + (1 - \alpha_u){u_e}^{k-1} \qquad (20)$$

In the Rhie and Chow scheme these cell-face velocity components are obtained explicitly through the interpolation of momentum equations for neighboring cell centered velocity components. After assuming few assumptions and solving the expression we get $u_e$ as:

$$
\begin{aligned}
u_e = [ & f_e u_E + (1 - f_e)u_P + (D_u)_e(P_P - P_E) \\
& - f_e(D_u)_E(P_w - P_e)_E - (1 - f_e)(D_u)_P(P_w - P_e)_P] \\
& + [(B_u)_e] - f_e(B_u)_E - (1 - f_e)(B_u)_P] \\
& + (1 - \alpha_u)[{u_e}^{k-1} - f_e {u_E}^{k-1} - (1 - f_e){u_P}^{k-1}] \qquad (21)
\end{aligned}
$$

where $f_e$ is the geometric interpolation factor defined in terms of distances between nodal points.

The term in the first set of brackets on the right-hand side of Eq. (21) is the original Rhie and Chow scheme. The term in the second set of brackets originated from the existence of a body force source term which in this case is the coriolis and centrifugal force, and the term in the last set of brackets is to obtain a converged solution that is independent of relaxation factors. A further detailed discussion about the Rhie Chow interpolation scheme can be found in [15] [16].

### 5.3.2   Under Relaxation Factor

Under relaxation factor is a parameter which is included when the velocities and pressures are corrected. When the expression for the velocity correction is derived, a term is neglected in the SIMPLE algorithm and hence an approximation is made. The neglected expression in the derivation is a term consisting of the velocity corrections of the neighbouring nodes of the considered cell centre which is unknown at that point. Once that is neglected as per the SIMPLE algorithm, the term left in the expression for velocity correction is a term consisting of pressure corrections. Hence, because of this omission, the pressure correction term is over burdened with the velocity correction as well. Making this approximation does not change the final solution but only alters the path to convergence.

Optimum under-relaxation factors are often problem dependent and a detailed discussion on selecting the under relaxation factors for solving the Navier Stokes equations can be found in [13]. In the present study, instead of correcting the velocity with the under relaxation factors in the end, we discretised the momentum equation in such a way that the under relaxation factors are implicitly present in the initial discretisation itself as depicted in Eq. (16) where $\alpha_u$ is the under relaxation factor used for the velocity in the X direction. Analogous equations were developed for the Y and Z momentum equations also respectively. But the pressure correction equation is a seperate entity and it has to be corrected with an under relaxation factor separately due to the issue of over burdening as mentioned above. Hence, the under relaxation factor for pressure is incorporated as mentioned below:

$$P = P^* + \alpha_P P' \tag{22}$$

where $P^*$, $\alpha_P$ and $P'$ are the guessed pressure, pressure under relaxation factor and the pressure correction respectively.

The values of the under relaxation factors for the present study were decided in reference to a similar study by H.F. Meier et al., J.J.N. Alves et al. and M. Mori et al. in [10]. It was found that the values of $\alpha_P$ greater than 0.2 diverges from the solution for any values of $\alpha_u$, while values less than 0.01 offer an extremely low convergence rate. Also $\alpha_u$ values

greater than 0.7 present the same results for all $\alpha_P$ values. Hence, $\alpha_P = 0.1$ and $\alpha_u = 0.8$ were chosen as the relaxation parameters for the present study.

## 5.4   Linear Equation Solver

An iterative method was used to solve the discretised equations over the 3D domain. In an iterative method, we guess a solution and use the equation to systematically improve it. In the present study we use the Conjugate Gradient Stabilized method (CGSTAB). Multiple solvers were tried to assess the rate of convergence and computational time before concluding to use CGSTAB, namely Gauss Seidel method and Stone's SIP method as explained below:

- Gauss Seidel method was tried out first due to the simplicity in it's technique and the small system memory requirement but the convergence rate of the solver was observed to be very slow resulting in larger number of iterations.

- Stone's SIP method was tried next and it was found to have a lesser computational time along with a relatively faster convergence rate but we decided not to go ahead with the same due to it's recursive algorithm which prevented us from parallel computing and also was found to require a large storing capacity in comparison to other iterative techniques.

Finally as explained above, the CGSTAB algorithm was implemented and it was observed to have a faster convergence rate compared to the other tested iterative techniques. A detailed expression of the CGSTAB algorithm can be found in [13]. The convergence was monitored with the residual. As explained in the flowchart above, we use the stored residuals of the momentum equations ($R_2{}^X$, $R_2{}^Y$, and $R_2{}^Z$)to monitor the convergence of the inner loops and the residual of the pressure ($R_2{}^P$) to monitor the convergence of external loop. Residual is given by :

$$Res = a_P \phi_P - \Sigma a_{nb} \phi_{nb} - S \tag{23}$$

The Euclidean norm of $R_2{}^P$ was used as the convergence criterion in the pressure-velocity coupling. The Euclidean norm can be expressed by

$$(R)_{ext.loop} = \sqrt{\sum_{i,j,k}(Res_{Pi,j,k})^2} \leq Tol \tag{24}$$

where the tolerance used was $10^{-13}$. For the inner looping, the convergence criterion used was a reduction of the initial value of the Euclidean norm of the residuals:

$$(R)_{innerloop} = \sqrt{\sum_{i,j,k}(Res_{momentumi,j,k})^2} \leq R_f R_0 \tag{25}$$

where $R_f$ is a reduction factor between 0.05 and 0.25, according to Kim and Ro (1995) and $R_0$ is the initial value of the Euclidean norm of the residuals as per [10].

# 6    RESULTS AND DISCUSSION

The sections so far give a summary of the pertinent literature and the techniques we opted after several rounds of literature survey and investigation. We used the C++ programming language as the software framework via which we created our mesh, implemented the mentioned boundary conditions to simulate the velocity profiles at different locations in our rotating channel.

However, to verify the implementation of our codebase, we tested out our program for the following system:

1. Rectangular pipeflow without rotation

In the following subsections, we present the results that we obtained under each of the aforementioned systems. The results of the test systems 1 are presented in subsections 1. After verifying our codebase, we implemented our program for our micro-channel with rotation.

## 6.1    Rectangular pipeflow without rotation

In the following system, we simulated the axial velocity profiles at different lengths along the channel. Since we employed a constant velocity at the inlet, no slip boundary condition at the walls, no penetration, and assumed an incompressible and viscous fluid flow, we anticipate a developing velocity profile along the z-direction that is explained as follows:

Let us consider fluid entering a rectangular pipe with uniform velocity. The fluid particles or more precisely the fluid particles in contact with the wall surfaces will come to a complete stop resulting in zero velocity. This is because of the no-slip condition at the wall surfaces. This layer also causes the fluid particles in the adjacent layer to slow down gradually as a result of friction. To make up for this velocity reduction, the velocity of the fluid in the mid-section of the pipe has to increase to keep mass flow rate throughout the pipe constant. Because of this, there is a formation of velocity gradient along the pipe.

The region of the flow in which the effects of viscous shearing forces are caused by fluid viscosity are felt are called as *velocity boundary layer*. This hypothetical boundary layer divides the flow in the pipe in two regions: *boundary layer region*, which viscous effects and velocity changes are significant and the irrotational flow region, in which the frictional effects are negligible and the velocity remains constant in the radial direction. The thickness of the boundary layer keeps increasing in the flow direction until the boundary layer reaches the pipe centre. The region from the pipe inlet to the point at which the boundary layer merges at the centre line is called the *hydrodynamic entrance region*, and the length of this region is **hydrodynamic entrance length** $(L_h)$. In this region, the velocity profile is not

| Type of fluid | Water |
|---|---|
| Temperature of fluid | 20°C |
| Dynamic Viscosity at **T = 20°C** ($\mu$) | $1 * 10^{-3} \frac{Ns}{m^2}$ |
| Kinematic Viscosity at **T = 20°C** ($\mu$) | $1 * 10^{-6} \frac{Ns}{m^2}$ |

Table 1: Properties of fluid in the pipe

| Shape of pipe | Cuboid |
|---|---|
| Pipe width | $4mm$ |
| Pipe height | $4mm$ |
| Pipe length | $700mm$ |
| Grid | $30 \times 30 \times 150$ |

Table 2: Dimensions and grid size of the pipe

fully developed but it is developing as a function of the pipe length. The region beyond the entrance region where the velocity profile is developed is called *hydrodynamically developed region.*

The shear stress at the pipe wall is related to the slope of the velocity profile at the surface. However, the velocity profile remains unchanged in hydrodynamically fully developed region that means wall shear stress also remains constant in that region. Conversely, in the hydrodynamic entrance region, wall shear stress is the highest at the pipe inlet where thickness of the boundary layer is the smallest. This wall shear stress gradually decreases till the fully developed region.

Figure 7 illustrates the velocity profile that we obtained from our simulation.

**Input parameters and pipe geometry characteristics:**

**Calculations:**

$$Let, Reynolds Number, R_e = 2000 (Laminar Flow) \tag{26}$$

$\bar{w}$ :

$$\frac{\rho \bar{w} D_H}{\mu} = 2000$$
$$\bar{w} = \frac{2000\mu}{\rho D_H}$$
$$= \frac{2000}{10^6 \times 4 \times 10^{-3}}$$
$$= 0.5 m s^{-1} \tag{27}$$

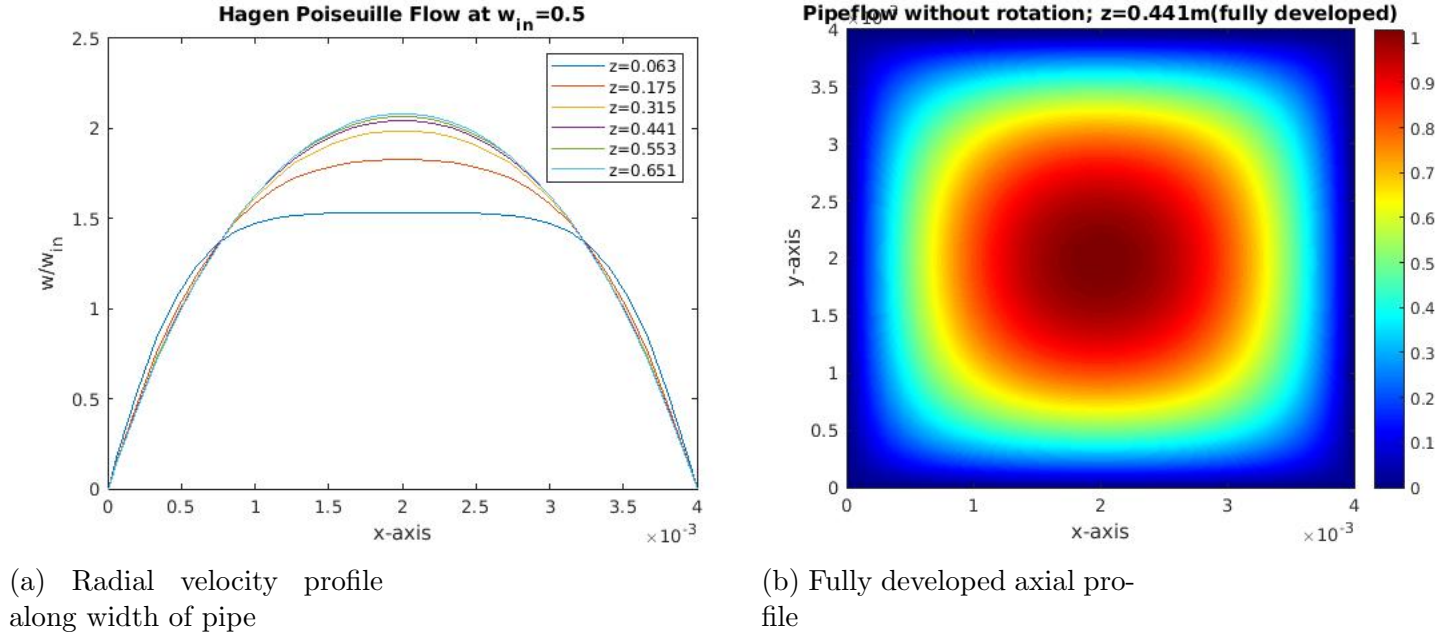(a) Radial velocity profile along width of pipe

(b) Fully developed axial profile

Figure 7: Axial velocity profile of a fluid in a stationary pipe

$L_h$ :

$$L_h \approx 0.05 R_e D_H$$
$$= 0.05 \times 2000 \times 4$$
$$= 400mm = 0.4m \tag{28}$$

**Parameters calculated so far:**

| Reynolds Number | 2000 |
|---|---|
| Average velocity | $0.5ms^{-1}$ |
| Hydrodynamic Length | 400mm |

Table 3: Fluid Parameters

In the figure 7(a), we see that the velocity at $z = 0.063m$ shows a large flat region centered at $y = 2mm$ indicating constant axial velocities. As the fluid progresses, we see that the region of constant axial velocity eventually develops fully at approximately $z = 0.441m$ centered at $y = 2mm$. The fluid is now said to be fully developed and the axial velocity profile remains unchanged as the fluid continues to flow.

The outlet was placed further downstream of the analytical hydrodynamic length (0.4m) so that it won't interfere with the values at the developing region. The comparison between analytical and numerical value of average velocity indicates good mass balance. Figure 7(a) shows the velocity profile in the hydrodynamically developed and developing region.

$$w_{avg} = \frac{\sum_{i=1}^{n} A_i w_i}{\sum_{i=1}^{n} A_i} \tag{29}$$

| Velocity $(ms^{-1})$ | Analytical Solution | CFD/Numerical Results | Error |
|---|---|---|---|
| Average velocity | 0.5 | 0.4995010098 | 0.00005 |

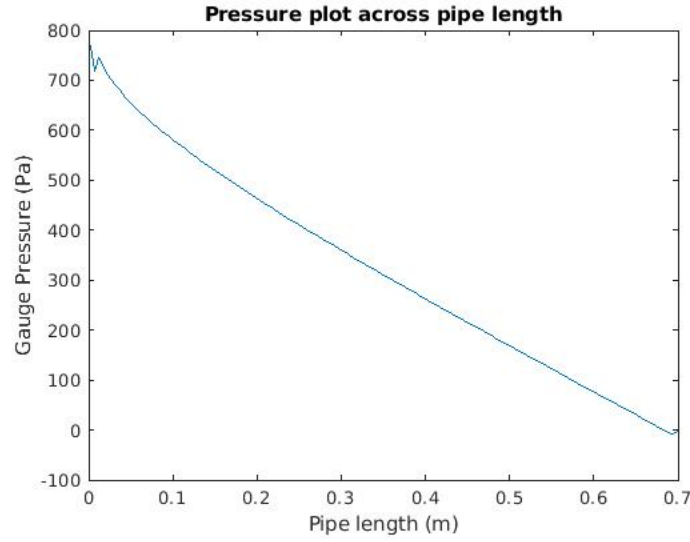Table 4: Analytical results vs Numerical Results



Figure 8: Pressure plot along the axial direction at $x = 0.002m, y = 0.002m$

Figure 8 indicates that the pressure decreases as a function of pipe length. The variation is non-linear in hydrodynamically developing region and linear in developed region as expected. We expect a more accurate solution after grid-independence study.

**Note:** Due to computational resource constraints and remote work setting owing to the COVID-19 pandemic, we were unable to conduct a grid independent study.

## 6.2   Rotating Micro-channel

In this subsection, we present the results we obtained through our simulation. A disc is rotated about an axis perpendicular to its face and through its centre. Several micro-channels are embedded on this disc as explained earlier. We take one such micro-channel and study the fluid flow properties through it.

Following are the details of the micro-channel:

| Shape of pipe | Cuboid |
|---|---|
| Micro-channel width | $0.2mm$ |
| Micro-channel height | $0.2mm$ |
| Micro-channel length | $20mm$ |
| Offset between disc centre and micro-channel entry | $20mm$ |
| Grid | $31 \times 31 \times 151$ |

Table 5: Dimensions and grid size of micro-channel

| Type of fluid | Water |
|---|---|
| Temperature of fluid | 20°C |
| Dynamic Viscosity at T = 20°C ($\mu$) | $1 * 10^{-3} \frac{Ns}{m^2}$ |
| Kinematic Viscosity at T = 20°C ($\mu$) | $1 * 10^{-6} \frac{Ns}{m^2}$ |

Table 6: Fluid properties in the micro-channel

Figure 9 and Figure 10 illustrates the development of axial velocity profile of the fluid as it flows through the micro-channel. In practical situations, the inlet velocity of the fluid cannot be specified. However, the average flow velocity is linked to the rotational speed.[17] This average speed is then taken as the inlet velocity.

The rotational Reynolds number and Reynolds number were chosen similar to how it was used in [17]. They have derived an approximate analytical expression relating the average velocity and angular velocity and this was used to arrive at the respective Reynolds numbers.

Graphs in Figure 7 were plotted using GNUplot. For Figure 9, Google sheets were used to scan and select cell values corresponding to a cross sectional plane and MATLAB was used to extract those values and plot the surface plots.

The plotted line graphs and surface plots of rotating micro-channels indicate the domination of secondary flows at high RPS. Due to this, we observed that there is a slight mass imbalance occurring within the micro-channel at high RPS. As observed in Figure 9 and Figure 10, with an increase in rotational Reynolds number, there is a visible change in the velocity profiles and the area under the graph for various z values and are not constant. The flow was ideally expected to be fully developed as we go along the length, but due to the secondary flow because of the effects due to rotation along with the constant outlet pressure boundary condition, a clear irregularity was observed.
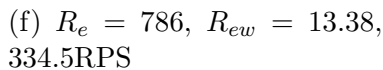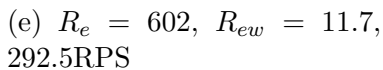
(a) $R_e = 12$, $R_{ew} = 1.67$, 41.75RPS

(b) $R_e = 49$ $R_{ew} = 3.34$, 83.5RPS

(c) $R_e = 110$, $R_{ew} = 5.02$, 125.5RPS

(d) $R_e = 442$, $R_{ew} = 10.03$, 250.75RPS

(e) $R_e = 602$, $R_{ew} = 11.7$, 292.5RPS
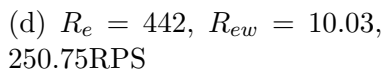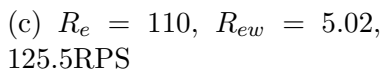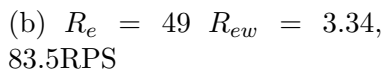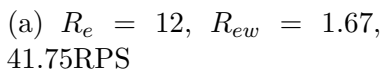
(f) $R_e = 786$, $R_{ew} = 13.38$, 334.5RPS
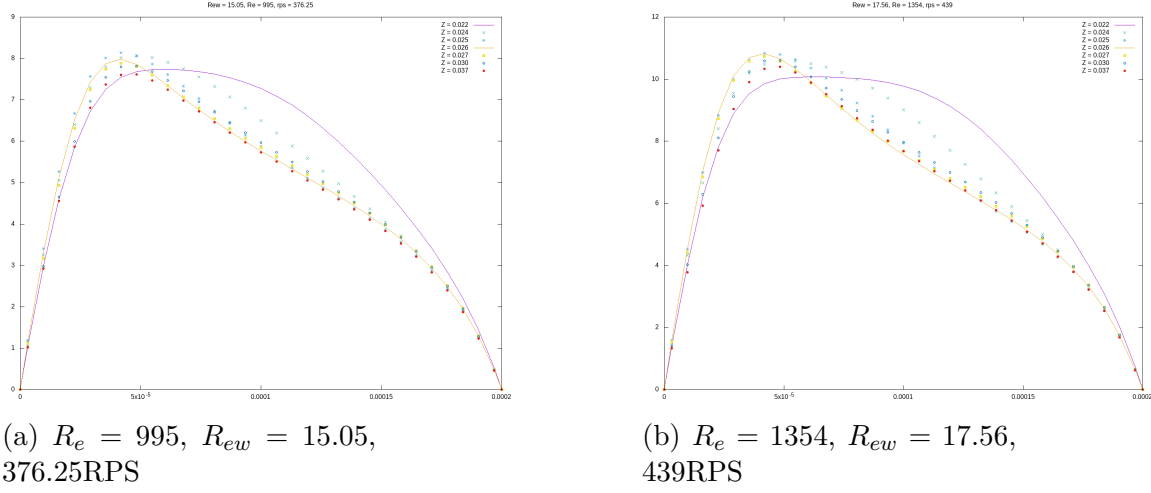
Figure 9: Axial velocity profile along width of the micro-channel for varying values of Reynolds Number Re
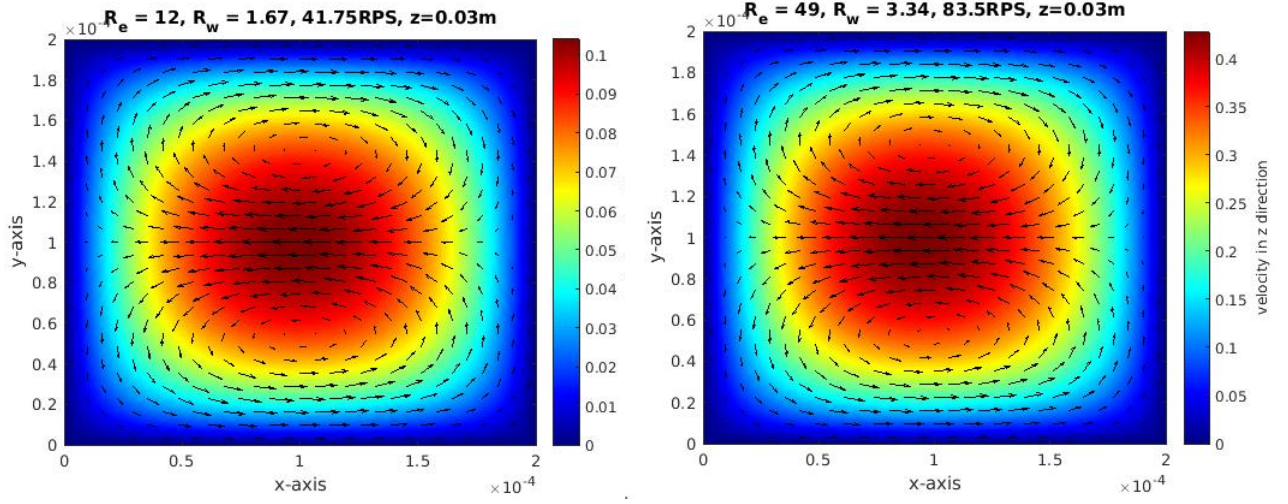
(a) Radial velocity profile
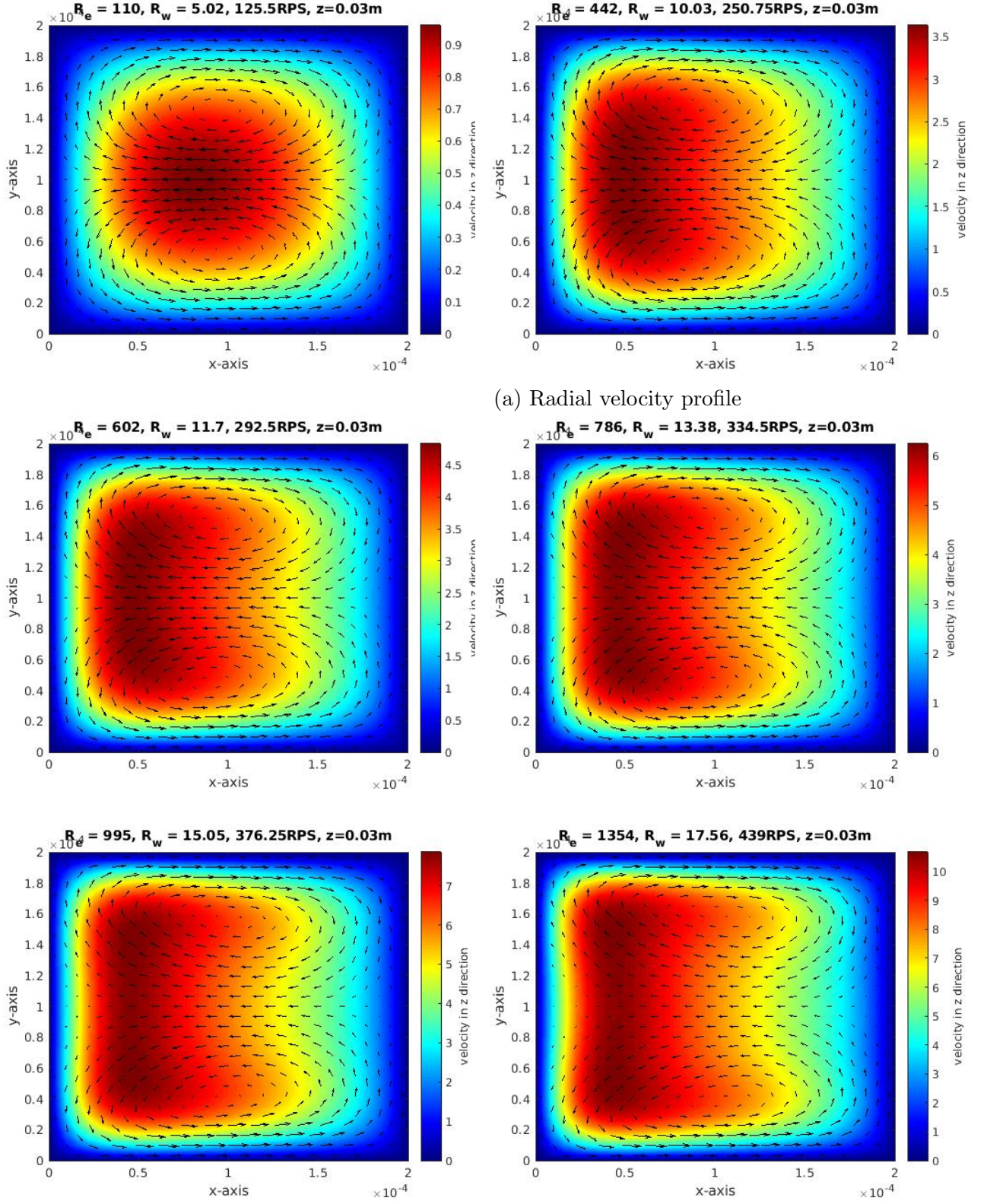
Figure 12: Axis velocity profile at z=0.03m at varying Reynolds Number Re. Vectors on the surface plot indicate the planar velocities. x and y axis are in meters

# 7 CONCLUSION AND FUTURE PROSPECTS

Pratanu Roy et al., N.K. Anand et al., and Debjyothi Banerjee et al., [17] has observed the pressure profile along the axial direction of the rotating micro-channel to be a near parabolic curve. Unlike the linear pressure variation in the developed region in normal rectangular pipeflow without rotation in figure 7, this requires a higher order extrapolation of pressure. However, instead of extrapolating the pressure, pressure correction based on mass conservation in the half cell at the outlet is expected to give better results.[16] Also, having a non-uniform grid with more nodes near the boundary would help in capturing the parabolic variation of pressure more accurately. The above mentioned alteration in boundary conditions and grid is part of the future work and is being implemented currently.

Once the necessary changes are made, we expect to derive a formula to find the entry length ($L_h$) in a rotating channel like how it is expressed for a normal pipe flow in Eq. (28) using Buckingham pi theorem. The non-dimensional analysis has revealed the entry length to be a function of non-dimensional parameters as mentioned below:

$$\frac{L_h}{D_H} = f(\frac{\rho \omega D_H^2}{\mu}, \frac{W}{\omega D_H}) \tag{30}$$

where $D_H$ - hydrodynamic diameter of the channel, $\omega$ - angular velocity of rotation, $\mu$ - absolute viscosity of the fluid, $\rho$ - density of the fluid, and W is the axial velocity of the fluid. It is clear from Eq. (30) that unlike the entry length for a normal pipe flow, the entry length for the rotating channel depends on the rotational Reynolds number which is the first non dimensional term and in turn the angular velocity which is also present in the second non-dimensional term. After running the simulation with the altered outlet boundary condition, the non-dimensional parameters corresponding to various test conditions has to be calculated and we intend to plot a graph showing the variation of $L_h$ with the 2 parameters found out from the Eq. (30) above. Regression analysis has to be done after the plotting the graph to estimate the relation between the entry length ($L_h$) and the 2 non-dimensional parameters. The relation is expected to be analogous to the structure of the Eq. (28) with the parameters being different in this case. Hence, the regression analysis should be done to find out the constant of proportionality and the mathematical relation binding $L_h$ with the 2 parameters.

Later on, mixing in micro-channel will be investigated using the code developed.

# References

[1] Pratanu Roy, N.K. Anand, and Debjyoti Banerjee. A review of flow and heat transfer in rotating microchannels. *Procedia Engineering*, 56:7–17, 12 2013.

[2] Abraham D. Stroock. Chapter 17 - microfluidics. In Frances S. Ligler and Chris Rowe Taitt, editors, *Optical Biosensors (Second Edition)*, pages 659–681. Elsevier, Amsterdam, second edition edition, 2008.

[3] H.A. Stone, Abraham Stroock, and A Ajdari. Engineering flows in small devices: Microfluidics toward a lab-on-a-chip. *Annu. Rev. Fluid Mech.*, 36:381–411, 01 2004.

[4] Abraham Stroock, Stephan Dertinger, Armand Ajdari, Igor Mezic, Howard Stone, and George Whitesides. Chaotic mixer for microchannels. *Science (New York, N.Y.)*, 295:647–51, 02 2002.

[5] Fadl Moukalled, Luca Mangani, and Marwan Darwish. Implementation of boundary conditions in the finite-volume pressure-based method—part i: Segregated solvers. *Numerical Heat Transfer, Part B: Fundamentals*, 69:1–29, 05 2016.

[6] Suhas Patankar. *Numerical heat transfer and fluid flow*. Taylor & Francis, 2018.

[7] A.W. Date. Solution of navier-stokes equations on non-staggered grid. *International Journal of Heat and Mass Transfer*, 36(7):1913–1922, 1993.

[8] A.W. Date. Fluid dynamical view of pressure checkerboarding problem and smoothing pressure correction on meshes with colocated variables. *International Journal of Heat and Mass Transfer*, 46(25):4885–4898, 2003.

[9] Sijun Zhang, Xiang Zhao, and Sami Bayyuk. Generalized formulations for the rhie–chow interpolation. *Journal of Computational Physics*, 258:880–914, 2014.

[10] H.F. Meier, J.J.N. Alves, and M. Mori. Comparison between staggered and collocated grids in the finite-volume method performance for single and multi-phase flows. *Computers Chemical Engineering*, 23(3):247–262, 1999.

[11] Henk Kaarle Versteeg and Weeratunge Malalasekera. *An introduction to computational fluid dynamics: the finite volume method*. Pearson education, 2007.

[12] S.V. PATANKAR and D.B. SPALDING. Paper 5 - a calculation procedure for heat, mass and momentum transfer in three-dimensional parabolic flows. In Suhas V. Patankar, Andrew Pollard, Ashok K. Singhal, and S. Pratap Vanka, editors, *Numerical Prediction of Flow, Heat Transfer, Turbulence and Combustion*, pages 54–73. Pergamon, 1983.

[13] Joel H Ferziger, Milovan Perić, and Robert L Street. *Computational methods for fluid dynamics*, volume 3. Springer, 2002.

[14] C. Rhie and W. Chow. Numerical study of the turbulent flow past an airfoil with trailing edge separation. *AIAA Journal*, 21:1525–1532, 1983.

[15] T. Miller and F. W. Schmidt. Use of a pressure-weighted interpolation method for the solution of the incompressible navier-stokes equations on a nonstaggered grid system. *Numerical Heat Transfer Part A-applications*, 14:213–233, 1988.

[16] Seok-Ki Choi, Seong-O Kim, CH Lee, and HK Choi. Use of the momentum interpolation method for flows with a large body force. *Numerical Heat Transfer Fundamentals*, 43:267–287, 03 2003.

[17] Pratanu Roy, N. Anand, and Debjyoti Banerjee. Numerical simulation of flow and heat transfer in radially rotating microchannels. *Microfluidics and Nanofluidics*, 15, 09 2013.